Reticulated Organic Photovoltaics

*Theanne Schiros, Stefan Mannsfeld, Chien-yang Chiu, Kevin G. Yager, James Ciston, Alon A. Gorodetsky, Matteo Palma, Zac Bullard, Theodore Kramer, Dean Delongchamp, Daniel Fischer, Ioannis Kymissis, Michael F. Toney, and Colin Nuckolls**

This paper shows how the self-assembled interlocking of two nanostructured materials can lead to increased photovoltaic performance. A detailed picture of the reticulated 6-DBTTC/C_{60} organic photovoltaic (OPV) heterojunction, which produces devices approaching the theoretical maximum for these materials, is presented from near edge X-ray absorption spectroscopy (NEXAFS), X-ray photoelectron spectroscopy (XPS), Grazing Incidence X-ray diffraction (GIXD) and transmission electron microscopy (TEM). The complementary suite of techniques shows how self-assembly can be exploited to engineer the interface and morphology between the cables of donor (6-DBTTC) material and a polycrystalline acceptor (C_{60}) to create an interpenetrating network of pure phases expected to be optimal for OPV device design. Moreover, we find that there is also a structural and electronic interaction between the two materials at the molecular interface. The data show how molecular self-assembly can facilitate 3-D nanostructured photovoltaic cells that are made with the simplicity and control of bilayer device fabrication. The significant improvement in photovoltaic performance of the reticulated heterojunction over the flat analog highlights the potential of these strategies to improve the efficiency of organic solar cells.

1. Introduction

Organic semiconductors have great promise to enable a new generation of low-cost, light-weight solar cells with thin and flexible form factors based on non-toxic, abundant materials. These features, along with the possibility to tailor emergent materials properties at the molecular level through synthesis, have the potential to improve photovoltaic device efficiency beyond present levels and make organic photovoltaics (OPV) an important component of future solar energy conversion technology.

Currently, bulk-heterojunction (BHJ) architectures, which are phase-segregated mixtures of semiconducting polymers and derivatized fullerenes, are the most efficient OPV devices.[1–3] The extended interface between intermixed phases of acceptor and donor molecules in a BHJ facilitates exciton dissociation, while the presence of continuous domains of each material facilitate transport of the separated charges to the electrodes. The nature of the interpenetrating nanostructure formed by the two semiconductors in the BHJ strongly influences the performance of organic solar cells because domain size, the nature of the interface, and molecular packing within each phase affect exciton dissociation, recombination, and charge transport. However, despite much work in this area, BHJ design remains largely Edisonian.[3,4]

The ability to design materials at the molecular level for self-assembly into controlled 3-D nanostructures represents a challenge with enormous potential to enable much higher OPV efficiency. We recently demonstrated how supramolecular

C.-y. Chiu, Dr. A. A. Gorodetsky,[†] Z. Bullard, Prof. C. Nuckolls
Department of Chemistry
Columbia University
NY, NY 10027, USA
E-mail: cn37@columbia.edu
Dr. T. Schiros, Prof. I. Kymissis
Energy Frontier Research Center
Columbia University
NY, NY 10027, USA
Dr. S. Mannsfeld, Dr. M. F. Toney
Stanford Synchrotron Radiation Light Source
Stanford Linear Accelerator Center
Menlo Park, CA 94025, USA
Dr. K. G. Yager, Dr. J. Ciston
Center for Functional Nanomaterials
Brookhaven National Laboratory
Upton, NY 11973, USA
Dr. M. Palma, T. Kramer
Department of Applied Physics and Mathematics
Columbia University
NY, NY 10027, USA
Dr. D. Delongchamp
Polymers Division
National Institute of Standards and Technology
Gaithersburg, MD 20899, USA
Dr. D. Fischer
Ceramics Division
National Institute of Standards and Technology
Gaithersburg, MD 20899, USA
[†] Current affiliation: Department of Chemical Engineering and Materials Science, The Henry Samueli School of Engineering, University of California, Irvine, Irvine, CA 92697 USA

DOI: 10.1002/adfm.201102572

self-assembly can be exploited for improved functional photovoltaic performance, utilizing p-type semiconductors derived from a family of contorted benzocoronenes as the electron donor.[5–7] Because of their doubly concave shape, these molecules form nested complexes with fullerenes in a "ball-and-socket" assembly motif.[5] We found that the dibenzotetrathienocoronenes (**6-DBTTC**, **Figure 1**A) derivatives of these molecules have power conversion efficiencies of ~2% for simulated sunlight (AM1.5) when they assemble into a reticulated heterojunction with C_{60} on transparent electrodes.[6] The fact that these efficiencies are four times higher than for flat, thermally evaporated analogs and approach the theoretical maximum for these materials (~3.5%) motivated a detailed study of the microstructure of the reticulated heterojunction that underlies the improved photovoltaic performance.[8]

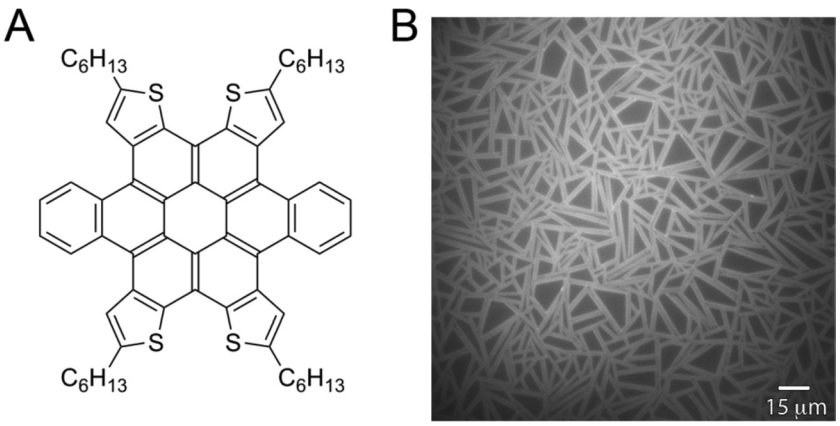

Figure 1. A) Molecular structure of **6-DBTTC**. B) Fluorescence micrograph of a network of **6-DBTTC** cables formed by a heat-induced self-assembly process.[6,7]

Here we present the details of the self-assembly of two crystalline nanostructured materials into a reticulated **6-DBTTC**/C_{60} heterojunction with interpenetrating donor and acceptor phases which underlies the increased device photovoltaic performance. The data show a structural and electronic interaction between the two materials at the molecular interface, and how molecular self- and directed- assembly can facilitate 3-D nanostructured photovoltaic cells that are made with the simplicity and control of bilayer device fabrication.

2. Results and Discussion

2.1. Self-Assembly and Microstructure of the 6-DBTTC Donor Layer

We found previously that optimal device performance occurred when a spin-cast film of the **6-DBTTC** (Figure 1A) was annealed on the surface of patterned electrodes prior to C_{60} deposition.[6] Figure 1B shows a typical fluorescence micrograph of a film of **6-DBTTC** on a PEDOT:PSS-coated ITO electrode after anneal at 150 °C.[6] The process for the formation of this structure involves two structural transitions. **6-DBTTC** is amorphous at room temperature and forms 1-D crystalline π-stacked fibers on annealing to around 100 °C. Temperature-dependent AFM reveals these fibers then coalesce into micrometer-size cables at 150 °C to form π-stacked, columnar superstructures that merge into a 3-D network of cables (shown in Figure 1B).[6]

We use GIXD to investigate the microstructure of pristine **6-DBTTC** films, spin-cast on ITO after heating to 150 °C. This would form the donor layer in the OPV device. The two-dimensional diffraction pattern provided in **Figure 2**A shows intense, sharp diffraction peaks confined to the lateral (q_{xy} or in-plane) and vertical (nominally q_z or out-of-plane) directions in reciprocal space, showing that the ensemble of cables (Figure 1B) is crystalline with strong fiber texture.[9] The peak positions correlate well to the diffraction pattern obtained for **6-DBTTC** single crystals.[6] In the single crystal, the molecules arrange into a columnar stack with a triclinic unit cell, as shown in Figure 2B. The single crystal diffraction pattern allows us to index the GIXD peaks of the donor layer and determine the crystallographic orientation and molecular packing of the π-stacked cables on the electrode surface.[10,11]

Figure 2A shows significant diffraction intensity confined along the nominally q_z (out-of-plane direction) between 0.3 and 0.4 $Å^{-1}$, corresponding to the periodic spacing (packing) of the 1-D molecular columns of which the cables are comprised. Increasing the intensity scale (inset of Figure 2A) shows the intensity is due to three distinct peaks at q_z = ~0.32, 0.34 and 0.36 $Å^{-1}$, which correspond to the (001), (100), and (01-1) reflections of the bulk structure, respectively. A complete indexing of the peaks indicates that each of the three peaks along q_z corresponds to a distinct crystallographic orientation in the film. Two examples are shown in Figure 2C.[12] These configurations are defined by the (001), (100) and (01-1) planes arranged parallel to the substrate and result in the observed out-of-plane diffraction intensity. Details of the analysis are provided in the Supporting Information (cf. Figure S2). The orientation of the π-stacking (high hole mobility) axis relative to the electrode substrate is different in the (001) and (01-1) cases (Figure 2C): nearly perpendicular in the (001) and parallel in the (01-1). While the three peaks in Figure 2A appear with similar intensity, the structure factor (obtained from the single-crystal diffraction measurement) is roughly four times lower for the (001) as compared to the other two peaks. We therefore estimate that the (001) orientation, with the more vertical substrate-relative π-stacking axis, is the dominant population. The important conclusion is that the donor layer consists of a crystalline **6-DBTTC** with a few distinct crystallographic orientations.

Figure S3 shows the near edge X-ray absorption spectroscopy (NEXAFS) at the C K-edge. This technique is sensitive to both chemical bond type and orientation at a film surface.[13–15] The results also indicate a preferentially edge-on orientation of the **6-DBTTC** molecules relative to the electrode substrate (Figure S3). Consistent with the three populations indicated by GIXD (Figure 2C), an azimuthal *average* molecular tilt angle of 64.2° ± 0.8 normal is estimated for the **6-DBTTC** film based on the angular dependence of the NEXAFS intensity (cf. Supporting Information Figure S3).[13]

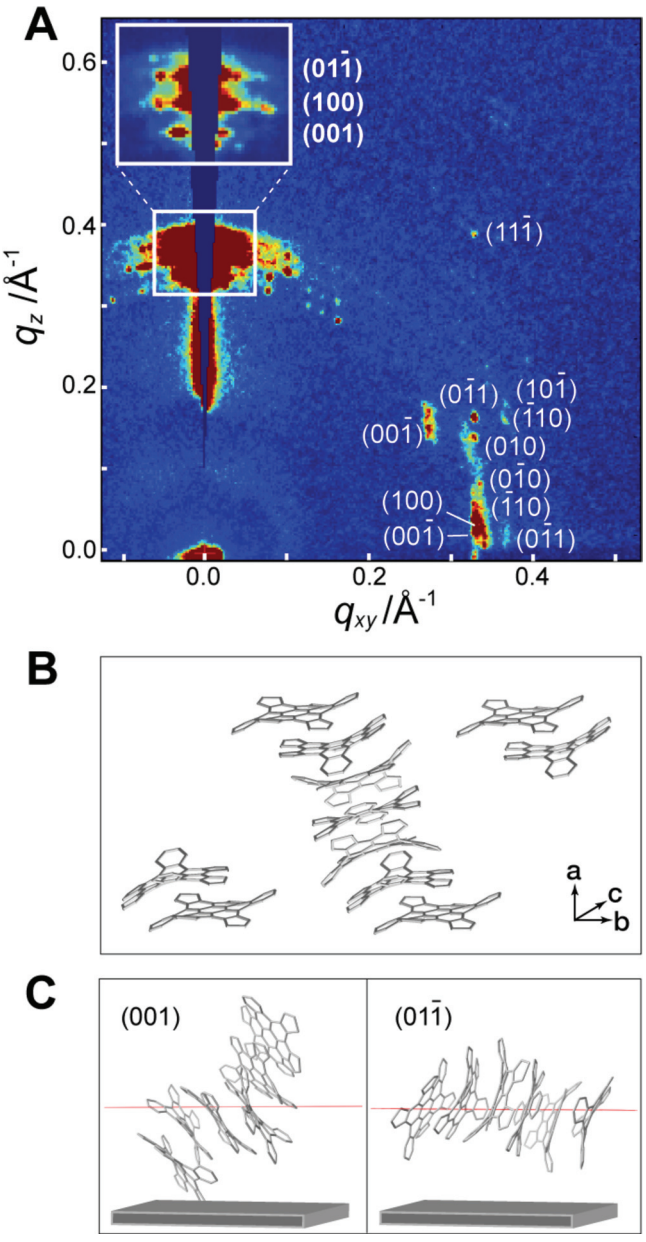

Figure 2. A) 2-D GIXD pattern for **6-DBTTC** films on ITO. B) **6-DBTTC** unit cell (full molecules are shown for ease of viewing) and a, b, and c crystallographic axes indicated. C) Two examples of distinct electrode-relative crystallographic orientations that coexist in the donor film; the red line indicates the unit cell lattice plane ((001) or (01-1)) which has diffraction intensity along the q_z direction (out-of-plane). The small peaks just off specular are due to the crossing and stacking of individual **6-DBTTC** cables (see Figure 1B) which twists the cables somewhat to rotate the spots left and right of the q_z axis.

2.2. Directed Assembly and Microstructure of the 6-DBTTC/C_{60} Reticulated Heterojunction

Having established the morphology and microstructure of the pristine **6-DBTTC** film, we turn our attention to the details of the donor-acceptor heterojunction formed when C_{60} is thermally evaporated onto the network of crystalline cables assembled on the surface of PEDOT:PSS-coated ITO electrodes. This is the next step in creating an OPV device.[6] To investigate the structure of this interface, we performed GIXD experiments for stepwise depositions of C_{60} of increasing thickness on the **6-DBTTC** cables, from 3 nm to the nominal device thickness of 40 nm. The results are summarized in **Figure 3**A where the diffraction intensity from a set of **6-DBTTC** diffraction peaks, corresponding to the packing of the molecular columns, is denoted "1" and that due to the (111) reflection of C_{60} is labeled "2".[16] Figure 3B shows the integrated intensity (in the region defined by the drawn arcs) from the **6-DBTTC** (1) and C_{60} (2) as a function of C_{60} thickness. When we evaporate C_{60} onto to the reticulated layers of **6-DBTTC**, we observe textured rings (at q ~ 0.77, 1.24 and 1.46 Å^{-1}) with intensity which increases with

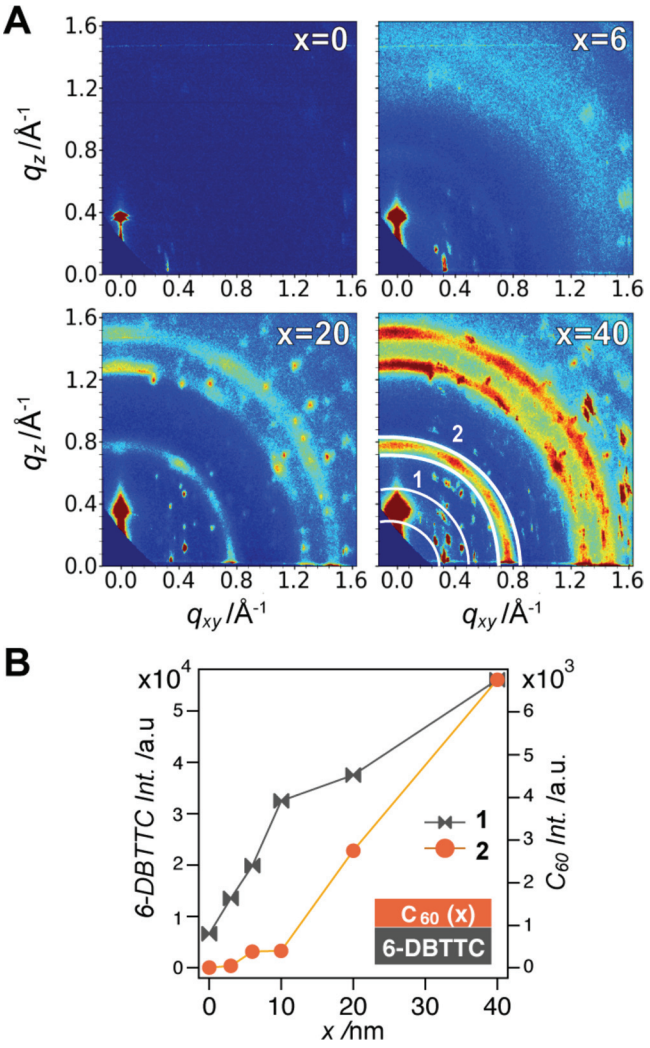

Figure 3. A) GIXD patterns for **6-DBTTC**/C_{60} heterojunction as a function of C_{60} deposition thickness (x) in nm, from x = 0 (pristine **6-DBTTC**) to x = 40 (nominal OPV device thickness) measured at a grazing incidence of 0.12°; the reference set of **6-DBTTC** peaks are labeled "1"; "2" denotes the (111) reflection of C_{60}. B) Diffraction intensity of **6-DBTTC** (1) and C_{60} (2) as a function of C_{60} deposition thickness integrated along the arcs defined in (A), as described in the text.

deposition thickness. However, a significant signal from the C_{60} is not observed until fairly thick layers (>10 nm) are deposited on the network of **6-DBTTC** cables; note the kink in the plot in Figure 3B. This behavior is different from that of the C_{60} layer deposited onto thermally evaporated films of **6-DBTTC** or hexabenzocoronene (HBC), where a C_{60} signal appears in the form of isotropic rings with intensity which increases roughly linearly with deposition thickness.[5] In those other cases the coronene donor films are flat and poorly crystalline.

For a typical organic bilayer, we would expect a decrease in diffraction intensity from the first layer as it is coated by the second. However, we instead observe a striking *increase* in the intensity, sharpness, and number (higher order) of **6-DBTTC** peaks -- and therefore in the crystalline order of the donor layer -- with increasing C_{60} thickness, even at 40 nm of C_{60} (Figure 3). Since the q-values of these sharp peaks are not shifted from the nominal q-values of the **6-DBTTC** crystal reflections, we do not attribute the increase to formation of a bimolecular co-crystal at the interface of molecular partners. Moreover, the strong enhancement of the **6-DBTTC** diffraction intensity introduced by deposition of C_{60} atop the donor film is observed for both short (~ ten micrometers in length (Figure 1B)) and long cables (hundreds of micrometers in length)[17] and for grazing incidence angles above and below the critical angle of the **6-DBTTC** film.[18] This shows conclusively that enhanced **6-DBTTC** crystallinity is not merely a surface phenomenon. Figure 3B shows this enhancement, as well as a kink in the intensity at 10 nm deposition thickness, at which point the rates of change in the diffraction intensity from the donor and acceptor layers switches, slowing for the **6-DBTTC** and increasing for the C_{60}.

The data provide mechanistic insight on the formation of the reticulated heterojunction, which we present schematically in **Figure 4**. Since the **6-DBTTC** diffraction exhibits enhanced crystallinity as a result of deposition of C_{60}, the pristine donor film must necessarily be partly amorphous; some of the molecules did not self-organize into the cable network crystallites during the limited (5 minute) anneal. We therefore begin with a **6-DBTTC** donor layer which is partly crystalline and partly amorphous (or semi-crystalline), shown in Figure 4A. We hypothesize that the deposition of C_{60} molecules imparts significant kinetic and thermal energy to the system, leading to further crystallization of the donor layer at the expense of the amorphous part of the **6-DBTTC** film, while the C_{60} phase separates into distinct regions that are in between cables, as shown in Figure 4B. This appears as a strong increase in diffraction intensity of the **6-DBTTC** and limited C_{60} diffraction signal for lower C_{60} depositions (<10 nm), as observed in Figure 3. At a certain transition point (~10 nm nominal C_{60} thickness), C_{60} layers form and the recrystallization of the **6-DBTTC** slows. This corresponds to the kink in Figure 3B, where we observe a marked increase in the C_{60} signal and a decline in the rate of enhancement of the **6-DBTTC** signal as a function of nominal C_{60} deposition thickness. This transition point is shown schematically in Figure 4C.

The increase in the diffraction from the C_{60} as a function of deposition thickness and the texture along the C_{60} rings (Figure 3A) can be understood as the fullerene filling the empty space in the 3-D supramolecular network of cables (see Supporting Information, Figure S5) to form partly oriented polycrystalline domains before forming a flat, polycrystalline capping layer. The intensity modulation along the C_{60} ring (Figure 3A) is evidence of the crystals being oriented; on flat thermally evaporated films of **6-DBTTC** and HBC we observe only isotropic diffraction rings from C_{60}.[5] AFM shows that the top surface of the heterojunction made from **6-DBTTC**/(40 nm) C_{60} is flat while surface-sensitive NEXAFS, which samples the top ~7–10 nm of the heterojunction, shows a pure C_{60} layer (Figure S4).[6]

We note that a phenomenon similar to that observed here may also occur in solution-processed polymer-fullerene BHJs upon thermal annealing (as opposed to thermal evaporation). For example, it was recently shown that PCBM rapidly diffuses into amorphous P3HT to make a mixed phase in P3HT-PCBM bilayers.[19,20] One hypothesis for such rapid diffusion is that PCBM plasticizes P3HT, which could have the effect of increasing its crystallinity.[21] Nonetheless, the important conclusion here is that the deposition of C_{60} strongly enhances the crystallinity of the **6-DBTTC** 3-D network, which in turn provides a scaffold that templates the fullerene acceptors into oriented polycrystalline domains.

Indeed, High Resolution Transmission Electron Microscopy (HRTEM) cross sections of the heterojunction show an interlocked, crystalline complex in agreement with the structure deduced from GIXD. We prepared the samples for the TEM using a focused ion beam (FIB) to mill the films into thin

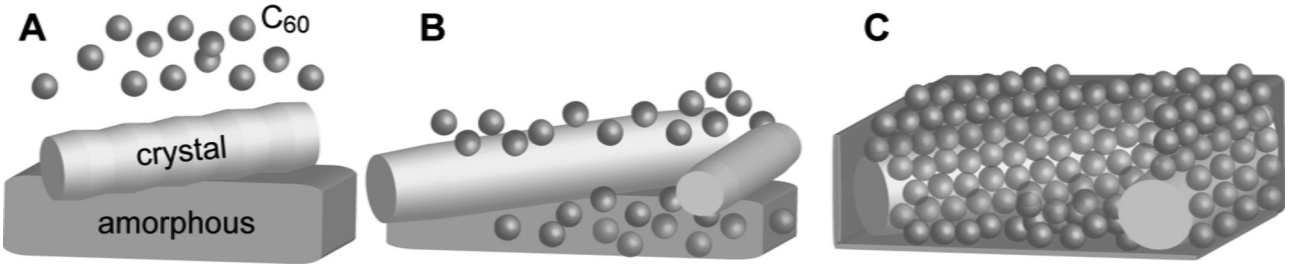

Figure 4. Schematic depiction of the formation of an interlocked charge transfer complex when C_{60} is thermally evaporated on **6-DBTTC** as described in the text: A) the pristine **6-DBTTC** film is semi-crystalline with some amorphous content; B) deposition of C_{60} molecules leads to further crystallization of the **6-DBTTC** film at the expense of the amorphous regions, while the C_{60} intimately mixes with the remainder; C) transition point at which polycrystalline C_{60} layers begin to form and the recrystallization of the **6-DBTTC** slows.

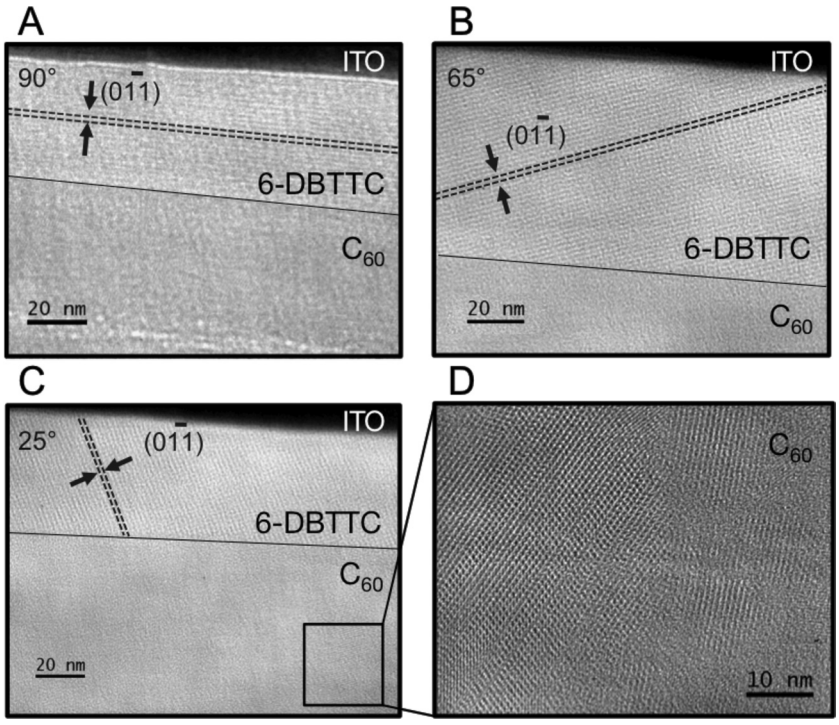

Figure 5. HRTEM images of a cross-section of a **6-DBTTC**/C_{60} heterojunction showing a single, unique π-stacking orientation, which is not necessarily along the fiber axis, for each of the three cables (A, B, C) in the FIB-generated cross-section. Each of three cables laying parallel to the ITO surface has a distinct orientation of the (01-1) reflection relative to the surface normal: A) 90°, B) 65° and C) 25°. D) Sufficiently thick (>20 nm) layers of C_{60} form polycrystalline films on **6-DBTTC**. A Wiener filter was applied to all images for noise reduction.

sections followed by a lift-out.[22] As shown in **Figure 5**, this technique enables us to directly visualize the 3-D reticulated heterojunction and connect the details of the morphology and microstructure at the level of a single **6-DBTTC** cable. Three individual crystalline **6-DBTTC** cables (which consist of many 1-D **6-DBTTC** fibers) oriented essentially parallel to the substrate with polycrystalline C_{60} filling the space in between cables (see Supporting Information Figure S5) were sampled in the FIB-generated cross-section. We observe that each of the three **6-DBTTC** cables is essentially a single crystallite with the 1-D molecular columns packed in a particular direction. However, the column orientation is not necessarily along the cable axis. In fact, of the three cables sampled we observe three distinct orientations of the (01-1) reflection (d = 17.8 Å, corresponding to the stacking of the **6-DBTTC** unit cell shown in Figure 2B) relative to the surface normal: 90º (Figure 5A), 65º (Figure 5B) and 25º (Figure 5C).[23] Therefore, the π-stacking (hole-transport) direction ranges from parallel (90º) to nearly perpendicular (25º) to the electrode contacts, with the crystallite length limited by the extent of the cable along the column axis (Figure 5). The TEM data are also consistent with the ensemble-averaged molecular orientation derived from NEXAFS (Figure S3) and the three preferential crystallographic orientations identified with GIXD (Figure 2). In the context of the device, the presence of interlocking donor and acceptor phases coupled with the higher crystallinity and multiple hole-transport axes relative to the electrodes leads to the increase in device performance.[6]

2.3. 6-DBTTC/C_{60} Molecular Interface

It is clear from the diffraction and electron microscopy that there is a structural interaction between the **6-DBTTC** and C_{60} molecules, but the remaining question is whether this is accompanied by a significant electronic interaction.[5,24,25] To address this we used XPS. **Figure 6** shows sulfur 2p (S 2p) XPS for pure **6-DBTTC** and the **6-DBTTC**/C_{60} (40 nm) OPV heterojunction. A shift of the S 2p XPS peak by 200 meV to lower binding energy for the heterojunction relative to pure **6-DBTTC** provides direct evidence of a significant electronic interaction between molecular donor and acceptor.[6] In particular, the binding energy shift indicates a change in screening of the core hole produced in the photoemission process. This shift is a fingerprint of an electrostatic interaction and charge displacement between the molecular partners.[26] The direction of the shift suggests fast charge transfer (within the lifetime of the S 2p core hole (<5 fs) from the **6-DBTTC** to the C_{60}; additional experiments are being performed to evaluate charge transfer rates.[5,25] The low mean free path of the electron in solids

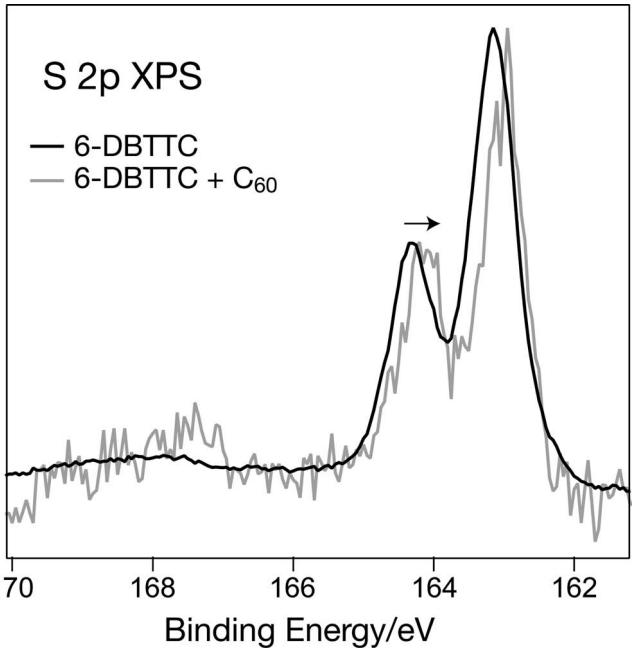

Figure 6. S 2p XPS for pristine **6-DBTTC** films on ITO (black) and with ~40 nm of C_{60} deposited on the **6-DBTTC** surface (grey); the latter represents the OPV heterojunction. Spectra were normalized to maximum peak height to facilitate comparison.

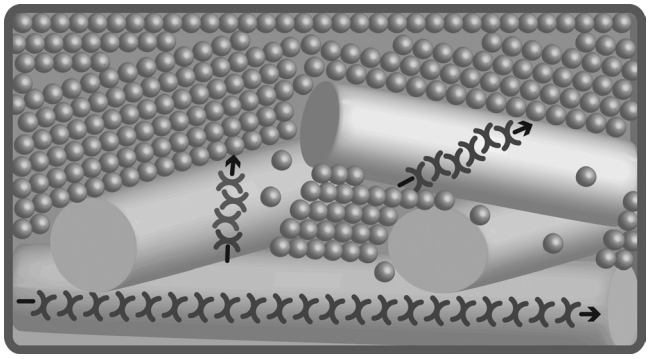

Figure 7. Schematic depiction of the **6-DBTTC**/C_{60} interlocked organic heterojunction, in which single crystal **6-DBTTC** cables form a 3-D scaffold to template a reticulated heterojunction with C_{60} (indicated by spheres). Doubly concave shapes indicate **6-DBTTC** to show molecular column packing relative to the cables, arrows indicate π-stacking (charge transport) direction.

results in a high surface sensitivity (~10 nm in the experimental conditions used here) and reduced signal-to-noise ratio for the C_{60} covered **6-DBTTC** samples (Figure 6).[27] The interpenetration of donor and acceptor phases in the 3-D heterojunction allows the **6-DBTTC** in the near-surface region to yield a detectable photoemission signal.

3. Conclusions

In summary, we have shown how the self-assembly of two crystalline nanostructured materials into a reticulated heterojunction with interpenetrating donor and acceptor phases can lead to increased device photovoltaic performance; more than an order of magnitude higher efficiency compared to active layers based on the flat, thermally evaporated analog.[6] The data, in particular the photoemission shift and the increase in **6-DBTTC** diffraction intensity in the heterojunction compared to the pristine layer, show that we not only have optimized the morphology between single crystal donor and polycrystalline acceptor but that there is also a structural and electronic interaction between them at the molecular interface. These findings are summarized in **Figure 7**, which shows a schematic representation of the **6-DBTTC**/C_{60} organic heterojunction, in which single crystal **6-DBTTC** cables, consisting of many 1-D molecular fibers, form a 3-D scaffold to template a reticulated heterojunction with C_{60} acceptors, facilitating both molecular assembly and efficient charge transfer at the interface.

4. Experimental Section

Grazing Incidence X-Ray Diffraction (GIXD): GIXD measurements were performed at the National Synchrotron Light Source (NSLS) of Brookhaven National Laboratory on beamline X-9 at and at Stanford Synchrotron Radiation (SSRL) Lightsource on beamline 11-3 at a photon energies of 14.0 keV and 12.7 keV, respectively. The incident x-ray beam, k_{in}, has a grazing incidence angle with the sample surface. A 2D MAR345 (pixel size of 0.15 mm) at SSRL or a Photonic Science WAXS detector (pixel size of 0.11 mm) at the NSLS, positioned a distance L from the sample, records the scattered beam, k_{out}. This is converted into an image of the reciprocal space (Q-space) with the scattering expressed as a function of the scattering vector $Q = k_{out}\text{-}k_{in}$. Here, the sample-to-detector distance L, calibrated with a LaB_6 polycrystalline standard, was 400.25 mm at beamline 11-3 (SSRL) and 265 mm at beamline X9 (NSLS). The samples were kept under a helium atmosphere at SSRL and in vacuum at NSLS during measurement to minimize damage to the films from the intense x-ray beam and eliminate x-ray scattering from air. Additional details are provided in the Supporting Information.

Near Edge X-ray Absorption Spectroscopy (NEXAFS): NEXAFS measurements were performed at the NIST (bending magnet source) beamline U7A of the National Synchrotron Light Source (NSLS) in partial electron yield (PEY) mode with a grid bias of –50 V. The reference absorption intensity (I_0) of the incoming x-ray beam, measured on a gold coated mesh positioned just after the refocusing optics, was measured simultaneously and used to normalize the spectra to avoid any artifacts due to beam instability. A linear background was subtracted from a region before the absorption edge and spectra were normalized with respect to carbon concentration by their intensity at 330 eV. Angle dependent NEXAFS data were obtained by changing the angle between the incoming x-ray beam and the sample incrementally from near parallel (20°) to near normal (70°) incidence; five angles are sufficient to obtain an accurate estimate of the average molecular orientation in the film based on the angular dependence of the 1s->π* transition.[15]

X-ray Photoelectron Spectroscopy (XPS): XPS measurements were performed at SSRL on beamline 13-2. Beamline 13-2 has a spherical grating monochromator and an energy range of 150–1100 eV, and the focused beam has a spot size of 0.01 × 0.075 mm^2. The XPS spectra were measured with energy resolution better than 100 meV. Sulfur 2p XPS was measured using photon energy 480 eV and the energy scale was calibrated using the C 1s peak position of C_{60} (285 eV).

High Resolution Transmission Electron Microscopy (HRTEM): TEM sample preparation was performed on an FEI Helios dual-beam FIB using a conventional cross-sectional liftout geometry. Final polishing was performed with a Ga^+ ion beam at 2 keV. HRTEM observations were performed on an FEI Titan equipped with a CEOS 3rd order geometric image aberration corrector at a primary beam energy of 80 keV and residual spherical aberration <2 µm. Transmission electron microscopy and diffraction were measured. An overview image of the TEM cross-section is provided in Figure S5, Fast Fourier Transforms (FFTs) corresponding to the TEM images in the main text are provided in the Supporting Information (Figure S6).

Epi-Fluorescence Microscopy: Epi-Fluorescence Microscopy (Epi-FM) followed the GIXD measurements on the same set of samples. Samples were transferred in inert atmosphere (N_2) from the diffraction experiment to microscopy measurements. Fluorescence measurements were performed using a microscope designed to accept glass substrates. An Olympus IX81 (Olympus, Inc.) inverted microscope equipped with a 40× air-objective and a 512 × 512 pixel Cascade II CCD Camera (Photometrics, Inc.) recorded the fluorescence images. The multi-channel mode was utilized, with excitation at 425 nm and emission at 605 nm for the green channel, excitation at 470 nm and emission at 525 nm for the red channel, and excitation at 570 nm and emission at 620 nm for the blue channel.

Supporting Information

Supporting Information is available from the Wiley Online Library or from the author.

Acknowledgements

Research supported as part of the Center for Re-Defining Photovoltaic Efficiency Through Molecular-Scale Control, an Energy Frontier Research Center funded by the U.S. Department of Energy (DOE), Office of Science, Office of Basic Energy Sciences under award number DE-

SC0001085. A. A. G. was supported by the National Science Foundation under Award Number CHE-0936923. Portions of this research were carried out at beamlines 11-3 and 13-2 at the Stanford Synchrotron Radiation Laboratory (SSRL), a national user facility operated by Stanford University on behalf of the U.S. Department of Energy, Office of Basic Energy Sciences, and at the Center for Functional Nanomaterials, and beamlines X-9 and U7A at the National Synchrotron Light Source (NSLS), Brookhaven National Laboratory, which are supported by the U.S. Department of Energy, Office of Basic Energy Sciences, under Contract No. DE-AC02-98CH10886. We thank Hirohito Ogaswara for assistance at beamline 13-2 and Kim Kisslinger for assistance with TEM sample preparation.

Received: October 25, 2011
Published online: January 19, 2012

[1] B. C. Thompson, J. M. J. Fréchet, *Angew. Chem. Int. Ed.* **2008**, *47*, 58.
[2] B. Kippelen, J. L. Brédas, *Energy Environ. Sci.* **2009**, *2*, 251.
[3] Y. Liang, Z. Xu, J. Xia, S.-T. Tsai, Y. Wu, G. Li, C. Ray, L. Yu, *Adv. Mater.* **2010**, *22*, E135.
[4] M. Green, K. Emery, Y. Hishikawa, W. Warta, *Prog. Photovolt: Res. Appl.* **2010**, *18*, 144.
[5] N. J. Tremblay, A. A. Gorodetsky, M. P. Cox, T. Schiros, B. Kim, R. Steiner, Z. Bullard, A. Sattler, W.-Y. So, Y. Itoh, M. F. Toney, H. Ogasawara, A. P. Ramirez, I. Kymissis, M. L. Steigerwald, C. Nuckolls, *ChemPhysChem* **2010**, *11*, 799.
[6] A. A. Gorodetsky, C.-Y. Chui, T. Schiros, M. Palma, M. Cox, Z. Jia, W. Sattler, I. Kymissis, M. Steigerwald, C. Nuckolls, *Angew. Chem. Int. Ed.* **2010**, *122*, 8081.
[7] C.-Y. Chiu, B. Kim, A. A. Gorodetsky, W. Sattler, S. Wei, A. Sattler, M. Steigerwald, C. Nuckolls, *Chem. Sci.* **2011**, *2*, 1480.
[8] A maximum conversion efficiency ($\eta = (J_{sc}*V_{oc}*FF)/100)$), where is J_{sc} is short circuit current, V_{oc} is open circuit voltage and FF is the fill factor, of 3.5% is computed based on estimates of the maximum value for each parameter. J_{sc} of 10 mA/cm^2 was calculated by integrating the absorbance spectrum of **6-DBTTC** with respect to the AM 1.5G solar spectrum and assuming and external quantum efficiency of 100%. V_{oc} equal to 0.7 V is estimated from the difference between the HOMO and LUMO levels of **6-DBTTC** and C_{60}, respectively, while a fill factor of 0.5 was assumed based on the maximum values reported for organic photovoltaic devices.
[9] J. L. Baker, L. H. Jimison, S. Mannsfeld, S. Volkman, S. Yin, V. Subramanian, A. Salleo, A. P. Alivisatos, M. F. Toney, *Langmuir* **2010**, *26*, 9146.
[10] J. A. Merlo, C. R. Newman, C. P. Gerlach, T. W. Kelley, D. V. Muyres, S. E. Fritz, M. F. Toney, C. D. Frisbie, *J. Am. Chem. Soc.* **2005**, *127*, 3997.
[11] D. Breiby, P. T. K. Chin, J. W. Andreasen, K. A. Grimsrud, Z. Di, R. A. J. Janssen, *Langmuir* **2009**, *25*, 10970.
[12] The intersection of the (100) plane with the **6-DBTTC** unit cell (and therefore the substrate relative column packing) is very similar to that of the (01-1) in this view as one is essentially a 90° rotation of the other.
[13] J. Stöhr, *NEXAFS Spectroscopy* (Eds: G. Ertl, R. Gomerand D. L. Mills), Springer-Verlag, **1992**, Ch. 3.
[14] D. M. DeLongchamp, E. K. Lin, D. A. Fischer, *Organic Field-Effect Transistors* (Eds: Z. Baoand, J. Locklin), CRC Press, Taylor & Francis Group, **2007**, Ch. 4.2.
[15] D. M. DeLongchamp, R. J. Kline, D. A. Fischer, L. J. Richter, M. F. Toney, *Adv. Mater.* **2010**, *23*, 319.
[16] In order to directly compare the diffraction patterns across the **6-DBTTC**/C_{60} series, a larger maximum value of the intensity scale was used than in Figure 2, so that in Figure 3 the diffraction peaks of the pristine **6-DBTTC** film appear to have lower intensity.
[17] The density and size of the cables can be controlled with temperature and anneal time. Annealing to 150 °C for five minutes or less produces a dense network of cables such as shown in Figure 1B, longer cables (up to mm in length) are formed for longer anneal time.
[18] The data shown in Figure 3 was measured at 0.12° grazing incidence at which the C_{60} signal is maximum.
[19] D. Chen, A. Nakahara, D. Wei, D. Nordlund, T. P. Russell, *Nano Lett.* **2011**, *11*, 561.
[20] N. D. Treat, M. A. Brady, G. Smith, M. F. Toney, E. J. Kramer, C. J. Hawker, M. L. Chabinyc, *Adv. Energy Mater.* **2011**, *1*, 82.
[21] S. Lilliu, T. Agostinelli, E. Pires, M. Hampton, J. Nelson, J. E. Macdonald, *Macromolecules* **2011**, *44*, 2725.
[22] L. A. Giannuzzi, F. A. Stevie, *Micron* **1999**, *30*, 197.
[23] Fast Fourier Transforms (FFTs) of the TEM images shown in Figure 5 are provided in the Supporting Information.
[24] G. Polzonetti, C. Battocchio, A. Goldoni, R. Larciprete, V. Carravetta, R. Paolesse, M. V. Russo, *Chem. Phys.* **2004**, *197*, 307.
[25] P. Vilmercati, C. Castellarin Cudia, R. Larciprete, C. Cepek, G. Zampieri, L. Sangaletti, S. Pagliara, A. Verdini, A. Cossaro, L. Floreano, A. Morgante, L. Petaccia, S. Lizzit, C. Battocchio, G. Polzonetti, A. Goldoni, *Surf. Sci.* **2006**, *600*, 4018.
[26] Such shifts are usually strongest for the 1s level and a measurable shift in a 2p level indicates that the electronic interaction is especially significant.
[27] C. Martin, E. T. Arakawa, T. A. Callcottand, J. C. Ashley, *J. Electron Spectrosc. Relat. Phenom.* **1985**, *35*, 307.